

Encapsulated X-Ray Detector Enabled by All-Inorganic Lead-Free Perovskite Film With High Sensitivity and Low Detection Limit

Hainan Zhang^{ID}, Guanhua Dun, Qixin Feng^{ID}, Rui Zhao, Renrong Liang^{ID}, Member, IEEE, Ziyuan Gao^{ID}, Thomas Hirtz^{ID}, Min Chen, Xiangshun Geng^{ID}, Mingyang Liu, Yao Huang, Xinran Zheng^{ID}, Ken Qin, Xichao Tan, Xuefeng Wang, Dan Xie, Associate Member, IEEE, Yi Yang, He Tian^{ID}, Member, IEEE, Yuanyuan Zhou, Nitin P. Padture, Xueyun Wang^{ID}, Jiawang Hong, and Tian-Ling Ren^{ID}, Senior Member, IEEE

Abstract—The sensitive detection of low-dose X-ray radiation is essential to many X-ray applications. In this article, the ultrasensitive X-ray detector based on pure $\text{Cs}_2\text{AgBiBr}_6$ all-inorganic lead-free perovskite film is successfully demonstrated and encapsulated using a metal casing with a Be window. The high-quality $\text{Cs}_2\text{AgBiBr}_6$ films are obtained through the low-cost solution process with long electron–hole diffusion length (~ 700 nm) and long carrier lifetime (~ 750 ns). Benefiting from the excellent properties of the $\text{Cs}_2\text{AgBiBr}_6$ film and the stable ambient provided by the packaging module, the resulting device exhibits attractive X-ray detection capabilities with a minimum detectable dose rate of $145.2 \text{ nGy}_{\text{air}} \text{s}^{-1}$ and a detection

sensitivity up to $1.8 \times 10^4 \mu\text{CGy}_{\text{air}}^{-1}\text{cm}^{-2}$, which is about a thousand times higher than the sensitivity achieved with commercial a-Se X-ray detectors. Besides, the encapsulated device maintains superior detection performance after 2 months of storage, indicating the favorable reliability of the encapsulated device. This article demonstrates a possibility to use $\text{Cs}_2\text{AgBiBr}_6$ perovskite film and Be window for the sensitive X-ray detection, which will inspire further development of radiation electronics by utilizing all-inorganic lead-free perovskite.

Index Terms—Encapsulation, perovskite film, photodetector, radiation electronics, X-ray.

Manuscript received March 24, 2020; revised May 17, 2020; accepted May 26, 2020. Date of publication June 8, 2020; date of current version July 23, 2020. This work was supported in part by the National Key Research and Development Program under Grant 2016YFA0200400 and Grant 2016YFA0200300, in part by the National Natural Science Foundation under Grant 51861145202, Grant 61874065, Grant 61574083, and Grant 61434001, in part by the National Basic Research Program under Grant 2015CB352101, in part by Special Fund for Agroscientific Research in the Public Interest of China under Grant 201303107, in part by the Research Fund from Beijing Innovation Center for Future Chip, in part by the Independent Research Program of Tsinghua University under Grant 2014Z01006, and in part by the Shenzhen Science and Technology Program under Grant JCYJ20150831192224146. The review of this article was arranged by Editor C. Surya. (Hainan Zhang, Guanhua Dun, and Qixin Feng contributed equally to this work.) (Corresponding author: Hainan Zhang.)

Hainan Zhang, Guanhua Dun, Renrong Liang, Thomas Hirtz, Xiangshun Geng, Mingyang Liu, Yao Huang, Ken Qin, Xichao Tan, Xuefeng Wang, Dan Xie, Yi Yang, He Tian, and Tian-Ling Ren are with the Institute of Microelectronics, Tsinghua University, Beijing 100084, China, and also with the Beijing National Research Center for Information Science and Technology (BNRist), Beijing 100084, China (e-mail: zhanghn_tsinghua@126.com; liangrr@tsinghua.edu.cn; xiedan@mail.tsinghua.edu.cn; renlt@tsinghua.edu.cn).

Qixin Feng and Xinran Zheng are with the Department of Physics, Tsinghua University, Beijing 100084, China.

Rui Zhao is with the National Institute of Metrology, Beijing 100029, China.

Ziyuan Gao, Xueyun Wang, and Jiawang Hong are with the Beijing Institute of Technology, Beijing 100081, China.

Min Chen, Yuanyuan Zhou, and Nitin P. Padture are with the Institute for Molecular & Nanoscale Innovation, School of Engineering, Brown University, Providence, RI 02912 USA.

Color versions of one or more of the figures in this article are available online at <http://ieeexplore.ieee.org>.

Digital Object Identifier 10.1109/TED.2020.2998763

I. INTRODUCTION

X-RAY detectors play a very important role in many fields, such as security detection, medical diagnostics, and industrial flaw detection. The solid-state semiconductor detectors, which directly convert X-rays into an electrical signal, have gained increasing attention due to their structure simplicity, compactness, and robustness, such as Si [1], Se [2], Cd(Zn)Te [3], [4], and diamond [5]. However, these materials suffer from persistent unsolved issues associated with difficulties encountered in the crystal growth or device performance [6]. Due to the lower average atomic number of Si, it is difficult to achieve effective X-ray absorption. For Cd(Zn)Te crystals, binary phases are often present during crystal synthesis, which will affect the local carrier transport properties [7]. Although these materials have been mostly investigated as X-ray converters, a-Se is the predominant direct converting material used in commercial devices due to its favorable integration with established readout electronics. Meanwhile, in order to further reduce the dose of ionizing radiation, many researchers have focused on improving the detection sensitivity and lowering the detection limit of the X-ray detectors. Besides the choice of detection materials, the device structure and the encapsulation mode are also critical to the X-ray detector. To achieve successful X-ray detection applications, some features should be considered within the overall framework.

- 1) X-ray absorption coefficient, α , of the material is determined by $(\alpha \propto Z^4/E^3)$ [8], where Z is the average atomic number, and E is the photon energy. Therefore, high- Z contributes to more effective radiation absorption.
- 2) Superior carrier transport characteristics help to achieve high-efficiency carrier transport and separation, such as long carrier lifetime τ , high mobility μ , and short carrier transit time τ_t .
- 3) Large intrinsic resistance enables low dark current, which helps to reduce the noise current and lower the detection limit of the detector.
- 4) Suppression of field-driven ion migration allows a larger bias voltage applied to the detector without a simultaneous increase in noise current.
- 5) Shorter carrier transit time is beneficial for greater gain factor G ($G = \tau/\tau_t$), resulting in a large detection sensitivity.
- 6) Applicable encapsulation mode is capable of blocking the external ambient and provides an inert atmosphere, thereby reducing the instability of the device.

In recent years, hybrid lead halide perovskite materials ABX_3 ($A = \text{CH}_3\text{NH}_3^+$ (MA^+), $\text{CH}(\text{NH}_2)_2^+$ (FA^+); $B = \text{Pb}^{2+}$; $X = \text{Cl}^-, \text{Br}^-, \text{I}^-$) have attracted widespread attention due to their great application potential in the field of radiation detection due to their high X-ray absorption coefficient, low carrier effective masses, long carrier recombination lifetime, and high carrier mobility [9]–[16]. For instance, both X-ray detectors based on MAPbI_3 films [10] and MAPbI_3 wafer [11] exhibit excellent X-ray detection performance with detection sensitivities of $1.1 \times 10^4 \mu\text{CGy}_{\text{air}}^{-1}\text{cm}^{-2}$ and $2.5 \times 10^3 \mu\text{CGy}_{\text{air}}^{-1}\text{cm}^{-2}$, respectively. Besides, the X-ray detector based on MAPbBr_3 single crystal [12] ($\sim 80 \mu\text{CGy}_{\text{air}}^{-1}\text{cm}^{-2}$) and the detector integrated MAPbBr_3 single crystal on silicon wafer [13] ($2.1 \times 10^4 \mu\text{CGy}_{\text{air}}^{-1}\text{cm}^{-2}$) are also demonstrated. It should be noted that the sensitivities of hybrid lead halide perovskite X-ray detectors mentioned above are much higher than those achieved with commercially available a-Se X-ray detectors [2]. Moreover, due to the outstanding tolerance to structural defects, as well as the excellent electronic and optical properties, hybrid lead halide perovskites have also been successfully served as solid-state gamma-ray detection materials [14], [16].

Although hybrid lead halide perovskites have exhibited many excellent properties, the poor stability of organic cations against heat and moisture, as well as the toxicity caused by lead (Pb), are two key issues limiting their further development. Therefore, searching stable and lead-free perovskite materials is the most straightforward strategy to solve this problem. Up to now, some studies have revealed that the thermal stability of perovskite materials can be greatly improved by replacing organic cations with Cs^+ [17]. When it comes to solving the problem of toxicity, the Sn^{2+} and Ge^{2+} metal cations, which possess the same outermost electronic structure as Pb^{2+} , are considered as alternatives to replace Pb^{2+} [18]. Unfortunately, Sn and Ge-based perovskites are extremely unstable and are easily oxidized in the air, limiting their practical applications [19].

Nowadays, a new category of perovskite material system, double perovskite with a general formula of $\text{A}_2\text{M}^+\text{M}^{3+}\text{X}_6$, provides a new solution to the toxicity and stability problem raised by hybrid lead halide perovskites. X is a halide; M^+ and M^{3+} are monovalent and trivalent cations, respectively. Up to now, some studies have reported the synthesis of double perovskite materials, including powders, single crystals, and films with bandgaps ranging from 1.83 to 2.45 eV [20], [21]. Based on the design framework of the X-ray detector above-mentioned, by using one Bi^{3+} and one Ag^+ to replace two Pb^{2+} , all-inorganic lead-free double perovskite $\text{Cs}_2\text{AgBiBr}_6$ has gradually become the focus of research in the field of radiation detection. Pan *et al.* [22] have successfully fabricated an X-ray detector based on $\text{Cs}_2\text{AgBiBr}_6$ single crystal with a low detection limit ($59.7 \text{ nGy}_{\text{airs}}^{-1}$), promoting the application of all-inorganic lead-free perovskites in radiation electronics. By introducing the phenylethylamine bromide into the precursor solution, the defect density in the $\text{Cs}_2\text{AgBiBr}_6$ single crystal is effectively reduced, resulting in a greatly improved X-ray detection sensitivity ($288.8 \mu\text{CGy}_{\text{air}}^{-1}\text{cm}^{-2}$) [23]. Besides, the photophysical pathways and carrier dynamics in $\text{Cs}_2\text{AgBiBr}_6$ single crystal have also been systematically studied by Steele *et al.* [24], substantially enhancing the recognition of the fundamental detection mechanism of the X-ray detector. However, in terms of $\text{Cs}_2\text{AgBiBr}_6$ single-crystal perovskite, it is still difficult to achieve large size growth, which hinders its integration with established commercial readout electronics, whereas the perovskite in the form of films has the potential to be prepared with a large area, low cost, and high quality. Meanwhile, the gain factor G of the current perovskite single-crystal X-ray detectors is relatively low with the values approximately ranging from 0.1 to 0.4 [12], [22]. For perovskite films, the carrier transit time can be greatly reduced by optimizing the film quality and the device structure. Since the $\text{Cs}_2\text{AgBiBr}_6$ perovskite materials are weakly p-type and contain defects, the photogenerated holes are transported, and electrons could be trapped [22]. When the transit time of the carrier is significantly shorter than its lifetime, the holes may traverse multiple times between the electrodes before recombination, which helps to achieve a larger X-ray detection sensitivity. Up to now, little research works related to $\text{Cs}_2\text{AgBiBr}_6$ film X-ray detector have been conducted, and the research on the detection mechanism of the X-ray detector based on perovskite film is still rarely explored. Furthermore, to the best of authors' knowledge, all previous perovskite X-ray detectors did not involve encapsulation, which is critical to the operation stability of the detectors. Therefore, it is particularly necessary and interesting to further research the use of $\text{Cs}_2\text{AgBiBr}_6$ perovskite film for X-ray detection applications and the X-ray detector encapsulation.

In this article, high-quality $\text{Cs}_2\text{AgBiBr}_6$ films are obtained through the systematical study of the best moment of dripping the antisolvent isopropanol (IPA) during the spin coating process. The results of X-ray diffraction (XRD) analysis and scanning electron microscope (SEM) show that the synthesized $\text{Cs}_2\text{AgBiBr}_6$ films are uniformly possessing pure phase and large grain size. The photophysical investigations reveal that

the $\text{Cs}_2\text{AgBiBr}_6$ film has a long carrier diffusion length of approximately 700 nm and a long carrier lifetime of nearly 750 ns. For the first time, the high-performance X-ray detector based on $\text{Cs}_2\text{AgBiBr}_6$ film with a planar photoconductive architecture is successfully demonstrated and encapsulated using a metal casing with a 100- μm -thick Be window. Benefiting from the excellent properties of the $\text{Cs}_2\text{AgBiBr}_6$ film and the stable ambient provided by the packaging module, the resulting encapsulated device exhibits attractive X-ray detection capabilities with a detection sensitivity up to $1. \times 10^4 \mu\text{CGy}_{\text{air}}^{-1}\text{cm}^{-2}$, which is higher than the sensitivity of a-Se detectors by several orders of magnitude. Besides, a minimum detectable dose rate of $145.2 \text{ nGy}_{\text{air}}\text{s}^{-1}$ is also achieved, which is much lower than that required for regular medical diagnosis ($5.5 \mu\text{Gy}_{\text{air}}\text{s}^{-1}$) [25]. Furthermore, the encapsulated device maintains superior detection performance after 2 months of storage, indicating the favorable reliability of the encapsulated device. This article demonstrates a possibility to use $\text{Cs}_2\text{AgBiBr}_6$ perovskite film and Be window for the sensitive X-ray detection, which will inspire further development of radiation electronics by utilizing all-inorganic lead-free double perovskite.

II. EXPERIMENTAL DETAILS

A. Substrate Preparation

A silicon wafer with a 300-nm-thick SiO_2 layer was used as the substrate, which was rinsed with acetone, alcohol, and deionized water before the device fabrication. A 50-nm-thick Au film was deposited on the silicon wafer as the electrode using standard photolithography and lift-off procedures with an interdigital shadow mask. The shadow mask was designed to be 3 μm in width and 700 μm in length with a neighboring finger spacing of 3 μm . Standard 1: One contact lithography processing was used in the experiment.

B. Preparation of Precursor Solution and Device Fabrication

First, the $\text{Cs}_2\text{AgBiBr}_6$ powders were added into dimethyl sulfoxide (DMSO) to prepare a precursor solution with a molar concentration of 0.55 M, followed by magnetic stirring at 85 °C for 10 h. After that, a clear yellow solution was obtained. The synthesis process of $\text{Cs}_2\text{AgBiBr}_6$ powders can be found in the previous work [30]. Second, the precursor solution was spin-coated on the silicon substrate (2000 rpm for 100 s) assisted by the antisolvent IPA dripping protocol. Both the precursor solution and the substrate were preheated to 85 °C. Subsequently, the film was placed into a vacuum chamber to promote rapid evaporation of solvents and annealed for 10 min at 280 °C in a nitrogen atmosphere. After the above processes, the X-ray detector based on the $\text{Cs}_2\text{AgBiBr}_6$ film with a planar photoconductive architecture was fabricated. About the encapsulation, the detector was encapsulated using a metal casing with a 100- μm -thick Be window to prevent an internal detector from being exposed to the outside environment. The inside of the metal casing was filled with nitrogen, a kind of inert gas, to reduce the influence of the external atmosphere (moisture or air) on the detector. The nitrogen pressure inside

the metal casing was slightly greater than one atmospheric pressure.

C. Characterization

The crystal structure of the $\text{Cs}_2\text{AgBiBr}_6$ perovskite film was examined by XRD (Bruker D8). The surface morphology of the film was characterized using an SEM (Cael Zeiss Microscopy, Merlin). Time-resolved photoluminescence (PL) measurements were conducted with a fluorescence spectrophotometer (Edinburgh Instruments, FLS980). A picosecond pulsed diode laser with a wavelength of 473.4 nm was selected as the excitation light source (Edinburgh photonics, EPL-470). The emission for time-resolved measurements was monitored at 640 nm being the wavelength of the maximum intensity of the steady-state photo-emission. For diffusion length, we assume that all the photogenerated carriers that reach the $\text{Cs}_2\text{AgBiBr}_6/\text{PC}_61\text{BM}$ or Spiro-MeOTAD/ $\text{Cs}_2\text{AgBiBr}_6$ interface will be quenched, and thus, the boundary conditions $N(L, t) = 0$ and $N(x, t) = N_0 \exp(-Ax/L)$ are used, where $x = L$ means the interface of quencher/ $\text{Cs}_2\text{AgBiBr}_6$, and A/L is the absorbance divided by $\text{Cs}_2\text{AgBiBr}_6$ thin-film thickness. Finally, the average diffusion lengths (L) of electrons and holes are calculated by $L = \sqrt{D\tau}$, where τ is the lifetime extracted without quenching layer and D is the diffusion coefficient, respectively. The X-ray source in the experiment was generated by an X-ray tube with a tungsten anode. Meanwhile, the radiation dose rate in the space atmosphere was accurately calibrated using a reference ionization chamber (Model: PTW-32002 and NIM-MEFAC-01, National Institute of Metrology, Beijing, China.). For electrical testing, the current–voltage (I – V) and current–time (I – T) curves were recorded using a semiconductor characterization system (Keithley, 4200-SCS) during the radiation.

III. RESULTS AND DISCUSSION

The X-ray detector developed in this article is based on $\text{Cs}_2\text{AgBiBr}_6$ perovskite film. We first calculated the X-ray absorption spectrum of the materials over a range of photon energies using the XCOM: photon cross section database [26] shown in Fig. 1(a). A larger absorption coefficient indicates that the material could absorb X-rays more effectively, making it possible to obtain a larger photocurrent. Without considering the resonance absorption edges of K , L , and M , the calculated absorption coefficient of $\text{Cs}_2\text{AgBiBr}_6$ is higher than the one of the MAPbBr_3 and MAPbI_3 and close to the value for CdTe over the entire energy range. These results are consistent with the average atomic number Z of the materials ($\text{Cs}_2\text{AgBiBr}_6 \sim 53.1$, $\text{MAPbI}_3 \sim 48.9$, and $\text{MAPbBr}_3 \sim 45.1$). In terms of stability, some studies have revealed that the thermal stability of perovskite materials can be greatly improved by replacing organic cations with Cs^+ . The results of thermogravimetric (TGA) [Fig. 1(b)] and differential scanning calorimetry (DSC) analyses [Fig. 1(c)] reveal that the $\text{Cs}_2\text{AgBiBr}_6$ not only shows no weight loss up to 450 °C but also no phase transition in the range of room temperature to 350 °C. Herein, high-quality $\text{Cs}_2\text{AgBiBr}_6$ films are synthesized through an optimized antisolvent spin

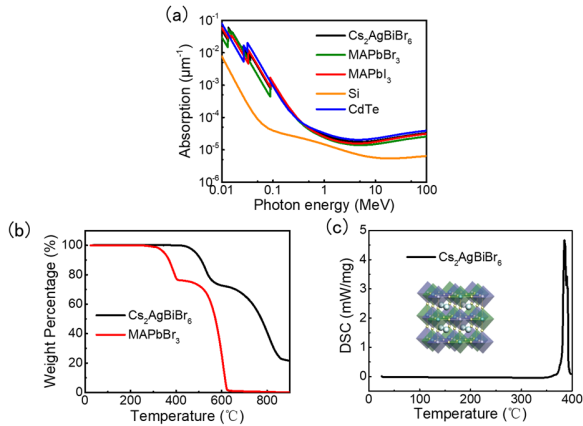


Fig. 1. (a) Theoretical absorption coefficient of several different materials as a function of photon energy ranging from 0.01 to 100 MeV. (b) TGA analysis of $\text{Cs}_2\text{AgBiBr}_6$ single crystal and $\text{MAPbBr}_3(\text{MA} = \text{CH}_3\text{NH}_3^+)$ single crystal. (c) DSC analysis of $\text{Cs}_2\text{AgBiBr}_6$ single crystal. (The inset in (c) shows the schematic of the atomic structure of $\text{Cs}_2\text{AgBiBr}_6$.)

coating method. The detailed description of film synthesis process can be found in the experimental details. The synthesis process of $\text{Cs}_2\text{AgBiBr}_6$ film can be roughly divided into three steps. First, the $\text{Cs}_2\text{AgBiBr}_6$ powders were added into DMSO to prepare a precursor solution with a molar concentration of 0.55 M, followed by magnetic stirring at 85 °C for 10 h. After this first step, a clear yellow solution was obtained. Second, the precursor solution was spin-coated on the silicon substrate (2000 rpm for 100 s) assisted by antisolvent IPA dripping protocol with both the precursor solution and the substrate preheated to 85 °C. Finally, the film was placed into a vacuum chamber to promote the rapid evaporation of solvents and annealed for 10 min in a nitrogen atmosphere. To completely transform the precursor into pure double perovskite phase, the annealing temperature needs to be higher than 250 °C [27], [28]. Therefore, the annealing temperature in this article was set to 280 °C.

During the synthesis of $\text{Cs}_2\text{AgBiBr}_6$ film, we systematically studied the best moment of dripping the antisolvent IPA and its effect on the morphology of the film. Fig. 2(a) shows the SEM top views of the $\text{Cs}_2\text{AgBiBr}_6$ film synthesized with the IPA dripping at different times, where the samples I, II, III, and IV are the films obtained by dripping IPA at 30, 40, 50, and 60 s, respectively. It can be found that with the delay of the IPA dripping time, the coverage of the perovskite film on the substrate was improved with larger grain size. At the same time, the SEM cross section view shows that the film is composed of a single layer of crystal grains. This single-layer morphology can greatly reduce the influence of grain boundaries on carrier transport along the longitudinal direction, leading to a high carrier transport efficiency in photodetection applications.

In order to determine the crystal structure of the $\text{Cs}_2\text{AgBiBr}_6$ film, XRD analyses of different samples were performed, and the results are shown in Fig. 2(b) and (c). The break coordinate at $\sim 32.99^\circ$ was used to eliminate the strong diffraction peak of the Si (200) plane from the substrate, which would make sample peaks difficult to discern.

The diffraction peaks of the all the $\text{Cs}_2\text{AgBiBr}_6$ film and $\text{Cs}_2\text{AgBiBr}_6$ powder matched well with the simulated pattern of cubic double perovskite structure (space group Fm-3m), indicating the pure phase of the samples. Furthermore, the full width at half maximum (FWHM) of the (004) diffraction peak decreases with the delay of IPA dripping time, which is consistent with the trend of the increasing average grain size of $\text{Cs}_2\text{AgBiBr}_6$ films. Such a trend of the average grain size from samples I–IV was also observed in the SEM analysis shown in Fig. 2(a). To understand the carrier dynamics of the $\text{Cs}_2\text{AgBiBr}_6$ film, the PL decay dynamics of different samples (I, II, III, and IV) were also performed, from which we can calculate the fluorescence lifetime of the carriers [Fig. 2(d)]. The carrier lifetimes of the samples (I, II, III, and IV) obtained by numerical fitting are 331.33, 574.16, 688.57, and 757.25 ns, respectively, which can be attributed to the reduction of grain boundaries in the perovskite film. Considering the thickness, grain size, film coverage, and carrier lifetime of $\text{Cs}_2\text{AgBiBr}_6$ films, 2000 rpm for 100 s with dripping antisolvent IPA at 60 s are considered as the optimal parameters for the synthesis of $\text{Cs}_2\text{AgBiBr}_6$ films. In order to estimate the electron/hole diffusion lengths in $\text{Cs}_2\text{AgBiBr}_6$ films, the PL decay dynamics [Fig. 2(e)] in a resulted film with and without quencher layers were also studied. The distributions of photogenerated electrons or holes $N_{e(h)}(x, t)$ in the $\text{Cs}_2\text{AgBiBr}_6$ film are described according to the improved diffusion-based equation including the electrostatic potential of the electrons/holes [29]

$$\frac{\partial N_{e(h)}}{\partial t} = I(x) + D_{e(h)} \frac{\partial^2 N_{e(h)}}{\partial x^2} + \frac{D_{e(h)}}{kT} \times \left(N_{e(h)} \frac{\partial^2 W_{e(h)}}{\partial x^2} + \frac{\partial W_{e(h)}}{\partial x} \frac{\partial N_{e(h)}}{\partial x} \right) - k_{\text{rec}} N_{e(h)} \quad (1)$$

where $D_{e(h)}$ is the diffusion coefficient for electrons or holes, and $I(x)$ is the excitation term. $W_{e(h)}$ is the electrostatic potential of the electrons or holes, and k is the Boltzmann's constant. T is the temperature, and k_{rec} is the PL decay rate. The calculated diffusion length for electrons is 774 and 663 nm for holes, and the calculated recombination rate for the carriers is the value of 10^6 – 10^7 s⁻¹, indicating potentially superior detection performance realized by $\text{Cs}_2\text{AgBiBr}_6$ film-based devices. The high-resolution transmission electron microscope (HRTEM) micrograph in Fig. 2(f) exhibits clear periodic fringes spacing of 0.332 and 0.235 nm, corresponding to (222) and (224) planes of $\text{Cs}_2\text{AgBiBr}_6$, respectively, illustrating the high quality of the as-prepared $\text{Cs}_2\text{AgBiBr}_6$ film.

To fabricate the detector, a silicon wafer with a 300-nm-thick thermal SiO_2 layer was used as the substrate, on which a 50-nm-thick Au interdigital electrode was deposited. Thereafter, the spin coating method was used to synthesize $\text{Cs}_2\text{AgBiBr}_6$ perovskite film with the aforementioned optimized synthesis parameters. Following the vacuum-assisted drying and the annealing process, the X-ray detector based on the $\text{Cs}_2\text{AgBiBr}_6$ film with a photoconductive planar architecture was fabricated. Energy-dispersive X-ray spectroscopy (EDX) measurements were performed to reveal the distribution of elements of the detector [Fig. 3(a)]. The EDX

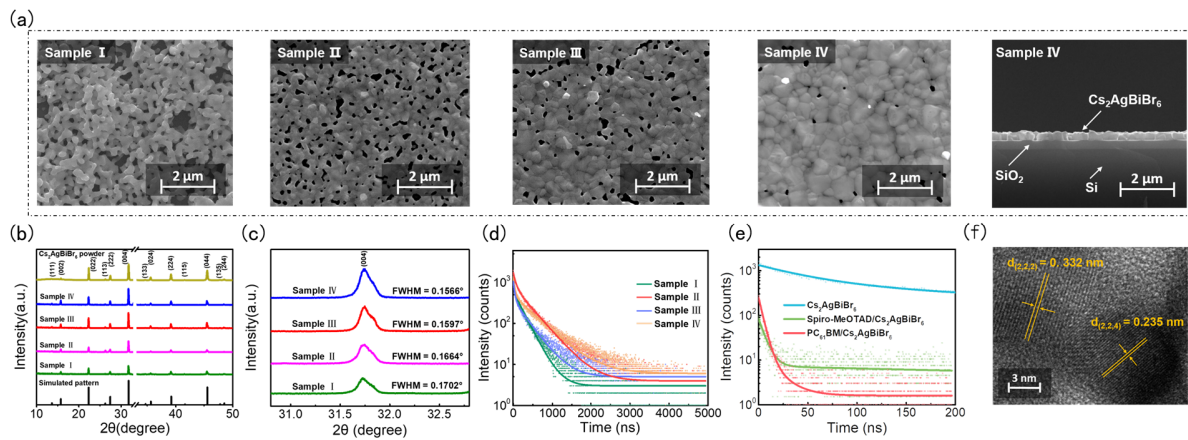


Fig. 2. Characterization of the $\text{Cs}_2\text{AgBiBr}_6$ perovskite film. (a) SEM top-view images of sample I, II, III, IV, respectively, and the cross section view image of sample IV. (b) XRD patterns of samples I, II, III, and IV and the $\text{Cs}_2\text{AgBiBr}_6$ powder synthesized in the experiment, compared with the simulated pattern of cubic double perovskite (bottom). (c) Magnified region of (004) diffraction plane. (d) PL decay dynamics of samples I, II, III, and IV, respectively, probed at 640 nm on an excitation at 470 nm. (e) PL decay dynamics in resulted optimized $\text{Cs}_2\text{AgBiBr}_6$ film with and without quenching layers. (f) HRTEM micrograph of the $\text{Cs}_2\text{AgBiBr}_6$ film prepared by the optimized synthesis process.

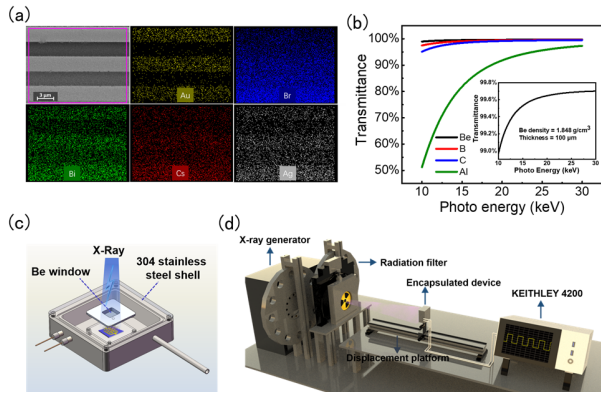


Fig. 3. Encapsulation of the device and the X-ray test platform. (a) EDX elements mapping of the detector with a 3- μm -spaced Au interdigital electrode. Au (yellow), Br (blue), Bi (green), Cs (red), Ag (white). (b) Transmittance of several different materials (100- μm thickness) to X-ray as a function of photon energy. (The inset in (b) is the X-ray transmittance of Be). (c) Schematic of the packaging module. (d) X-ray test platform.

mapping results show that the elements (Cs, Ag, Bi, and Br) are uniformly distributed on the substrate with Au electrodes.

In terms of encapsulation, the detection window is critical for X-ray detection, which should possess high X-ray transmittance as well as the good ability to block the visible and infrared light. We calculated the relationship between the transmittance of the X-ray and the photon energy with a fixed thickness (100 μm) of different materials using the Database: X-ray Interactions with Matter [31]. As shown in Fig. 3(b), Be has the highest transmittance to X-rays, which exceeds 99.7% for the X-ray with photon energies above 30 keV, indicating that the 100- μm -thick Be window has almost no attenuation to the incident X-ray. Due to the high transmittance to X-rays, favorable optical properties, and excellent mechanical strength and ductility, Be has become an essential material in the radiation detection window. Therefore, in the experiments, to prevent the detector from being exposed to external ambient, the $\text{Cs}_2\text{AgBiBr}_6$ film X-ray detector was encapsulated using a

304 stainless steel shell with a 100- μm -thick Be window. The schematic of the packaging module is shown in Fig. 3(c), and the inside of the packaging module was filled with nitrogen, a kind of inert gas, to reduce the influence of the external ambient (moisture or air) on the detector. The complete X-ray test platform is shown in Fig. 3(d). A tungsten anode X-ray tube with a photon energy up to 100 keV of Bremsstrahlung radiation was used in the experiment. The X-ray radiation dose rate in the air (air KERMA of the radiation) has been accurately calibrated by the reference ionization chambers. By adjusting different radiation filters, modulating the currents of the X-ray tube, and changing the distance between the device and the X-ray source, X-rays with different effective energies and different radiation dose rates in the air can be obtained.

The schematic of the device is shown in Fig. 4(a). When X-ray photons strike on the device, the electrons in the valence band will be excited to the conduction band, generating electron-hole pairs. These generated electron-hole pairs can drift rapidly under an applied electric field and then be collected by electrodes at both ends, thereby forming the photocurrent. First, we exposed the device to the X-rays with an effective energy (E_{eff}) of 39 keV, and the radiation dose rate in air ranges from 104.2 to 937.7 $\mu\text{Gy}_{\text{air}}\text{s}^{-1}$. Due to the lower photon energy of the X-ray and the larger average atomic number of the $\text{Cs}_2\text{AgBiBr}_6$ film, the interaction between the X-ray photons and perovskite film is composed of photoelectric effect and few Compton scattering. The current-voltage ($I-V$) characteristics of the device under dark conditions and different radiation dose rates are shown in Fig. 4(b). Due to the large intrinsic resistance of the $\text{Cs}_2\text{AgBiBr}_6$ film, the dark current of the device is maintained at a very low level under a large electric field intensity (5 V/3 μm), which is about several hundred pA. Periodic current-time ($I-T$) photore-sponse testing reveals the high repeatability of the device under different X-ray radiation dose rates shown in Fig. 4(c). It can be estimated that the rise time (τ_r) and fall time (τ_f) of the device under the radiation dose rate of 520.9 $\mu\text{Gy}_{\text{air}}\text{s}^{-1}$ are

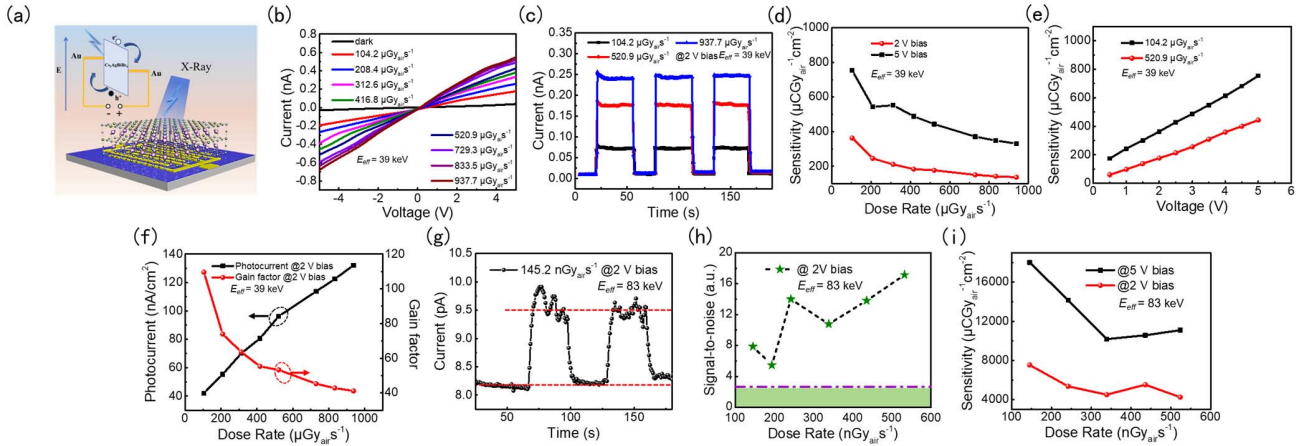


Fig. 4. X-ray detection performance of the encapsulated device. (a) Schematic of the structure of the $\text{Cs}_2\text{AgBiBr}_6$ film X-ray detector. (b) I - V characteristics of the encapsulated device under dark condition and different irradiation dose rates. (c) I - T response of the encapsulated device at different radiation dose rates. (d) Relationship between the sensitivity of the device and the X-ray radiation dose rate under different bias voltages. (e) Sensitivity of the device as a function of bias voltage under different radiation doses. (f) X-ray photocurrent and gain factor of the encapsulated device as a function of dose rate. (g) Device photoresponse to X-ray on tuning the X-ray source on and off (dose rate: $145.2 \text{ nGy}_{\text{air}} \text{s}^{-1}$). (h) Calculated SNR of the device as a function of X-ray radiation dose rate. (i) Relationship between the sensitivity of the encapsulated device and the X-ray radiation dose rate under different bias voltages.

about 1.042 and 1.581 s, respectively. The detection sensitivity is one of the key parameters for evaluating the X-ray detectors, which can be calculated by the following formula:

$$R = \frac{I_p - I_d}{D * s} \quad (2)$$

where I_p and I_d are the photocurrent and dark current, respectively. D refers to the radiation dose rate in air of the X-ray, and s represents the effective area of the detector (0.0021 cm^2). The detection sensitivities of the device as a function of radiation dose rates and bias voltages are shown in Fig. 4(d) and (e), respectively. It should be noted that the detection sensitivity tends to decrease with the increase of the X-ray radiation dose rate, which is consistent with the previous trend of $\text{Cs}_2\text{AgBiBr}_6$ single-crystal X-ray detectors [30]. This phenomenon can be explained as carriers gradually fill into shallower traps and the carrier recombination rate rises due to the increasing radiation intensity, leading to a decrease in sensitivity [22], [32]. On the contrary, the detection sensitivity of the device increases with the increasing applied bias voltage, which is mainly due to the enhancement of the collection efficiency of the photogenerated carriers. Therefore, increasing the bias voltage of the device is one of the effective ways to improve the detection sensitivity. Benefiting from the excellent X-ray absorption of the $\text{Cs}_2\text{AgBiBr}_6$ and superior carrier transport characteristics of the device, the detection sensitivity can reach up to $754.11 \mu\text{CGy}_{\text{air}}^{-1}\text{cm}^{-2}$ under a 5-V bias for X-rays with an effective energy of 39 keV. Besides the sensitivity, we also focus on the gain factor of the device. The gain factor G , which is considered as the carrier collection efficiency, can be calculated using the following formulas:

$$G = \frac{A_1}{A_0} \quad (3)$$

$$A_1 = \frac{I_p - I_d}{s * e} \quad (4)$$

$$A_0 = D \left(\frac{\mu_{\text{en}}}{\rho} \right)^{-1}_{\text{air}} \times \frac{(1 - \exp(-(\mu_{\text{en}})_{\text{Cs}_2\text{AgBiBr}_6} \times L))}{\Delta E} \quad (5)$$

where A_1 represents the number of charges actually collected by the electrodes at both ends in unit area and unit time. A_0 refers to the number of charges that the device can theoretically generate under X-ray irradiation (in unit area and unit time). e is the electron charge. $(\mu_{\text{en}}/\rho)_{\text{air}}$ represents the mass energy-absorption coefficient in air, which is about $6.833 \times 10^{-2} \text{ cm}^2/\text{g}$ for X-ray with the photon energy of 39 keV [33]. $(\mu_{\text{en}})_{\text{Cs}_2\text{AgBiBr}_6}$ refers to the linear energy-absorption coefficient of $\text{Cs}_2\text{AgBiBr}_6$, which is calculated to be 42.359 cm^{-1} . ΔE is the ionization energy of the electron-hole pair, and L is the thickness of the $\text{Cs}_2\text{AgBiBr}_6$ film. The gain factor in Fig. 4(f) is approximately 50 for the dose rate ranging from 416.8 to $937.7 \mu\text{Gy}_{\text{air}} \text{s}^{-1}$, similar to the value of the MAPbI_3 film X-ray detector [9].

A great number of applications related to radiation detection urgently need to reduce the radiation dose, particularly in the fields of medical diagnoses [12] and security inspections [34]. Lowering the detection limit of the detector can reduce the radiation dose, thereby reducing the potential biological risk of the X-ray. Therefore, the detection limit is also one of the figures of merit that are critical to assess the performance of the X-ray detector. By adjusting the radiation filter and the X-ray tube current, the X-ray with radiation dose rate in air of several hundred $\text{nGy}_{\text{air}} \text{s}^{-1}$ can be obtained with an effective energy of 83 keV. The I - T characteristics of the device are shown in Fig. 4(g). It can be seen that the photocurrent exhibits greater fluctuations than the dark current, which can be attributed to the ripple in the voltage waveform of the X-ray tube [35] and random electron-hole pair generation or recombination in the photoelectric process [22]. The IUPAC defines the detection limit as an equivalent radiation dose rate [36], which can produce a radiation signal current (I_{signal}) greater than three times of the noise current (I_{noise}). Therefore, we defined the detection limit as the radiation dose rate when

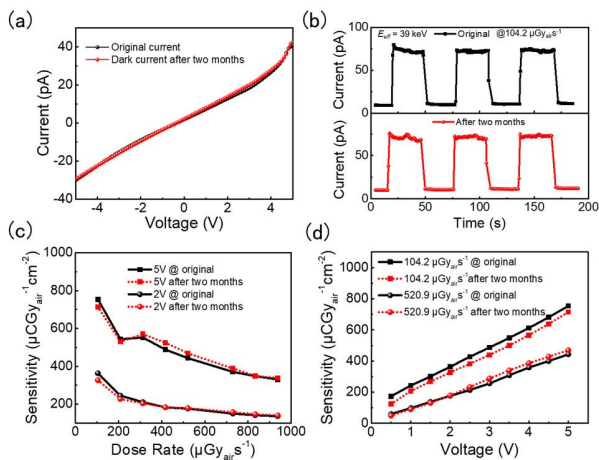


Fig. 5. Long-term stability test of the encapsulated device. (a) Original dark current and the dark current after 2 months of storage of the encapsulated device. (b) Periodic I - T photoresponse of the encapsulated device before and after 2 months of storage. (c) and (d) Comparison of the original sensitivity and the sensitivity after storage for 2 months of the encapsulated device.

the signal-to-noise ratio (SNR) is 3 at a given bias voltage. The SNR can be calculated by the following formulas:

$$\text{SNR} = \frac{I_{\text{signal}}}{I_{\text{noise}}} \quad (6)$$

$$I_{\text{signal}} = \bar{I}_{\text{photo}} - \bar{I}_{\text{dark}} \quad (7)$$

$$I_{\text{noise}} = \sqrt{\frac{1}{N} \sum_{i=1}^N (I_i - \bar{I}_{\text{photo}})^2} \quad (8)$$

where \bar{I}_{photo} and \bar{I}_{dark} represent the average photocurrent and average dark current, respectively. I_{noise} can be obtained by calculating the standard deviation of the photocurrent. For example, as shown in Fig. 4(g), the calculated I_{signal} and I_{noise} were 1.308 and 0.166 pA, respectively, at 2-V bias under $145.2 \text{ nGy}_{\text{air}}\text{s}^{-1}$, resulting in an SNR value of 7.88. Therefore, the actual lowest detection limit could even be smaller than $145.2 \text{ nGy}_{\text{air}}\text{s}^{-1}$. Furthermore, we also calculated the SNR under different radiation dose rates with a fixed bias voltage as shown in Fig. 4(h). The achieved superiorly low detection limit is comparable to those of the latest perovskite single crystal [12], [13], [22] and the perovskite-like single-crystal X-ray detectors [37], which are much lower than that required for regular medical diagnosis ($5.5 \mu\text{Gy}_{\text{air}}\text{s}^{-1}$). Such a low detection limit ($< 145.2 \text{ nGy}_{\text{air}}\text{s}^{-1}$) is mainly due to its extremely low dark current and still possesses room to be further improved in the future. Similarly, the detection sensitivity at a lower radiation dose rate was also derived as shown in Fig. 4(i), which can reach up to $1.8 \times 10^4 \mu\text{CGy}_{\text{air}}^{-1}\text{cm}^{-2}$ under a 5-V bias for X-ray with an effective energy of 83 keV, far beyond the value of the $\text{Cs}_2\text{AgBiBr}_6$ single-crystal X-ray detector. It is worth noting that, if it is an all-inorganic lead-free perovskite X-ray detector or the hybrid lead halide perovskite X-ray detector, their detection sensitivities are much higher than the sensitivity achieved with a-Se X-ray detectors [2] by several orders of magnitude.

To further demonstrate the long-term stability of the encapsulated device, the dark current as a function of voltage was measured after 2 months of storage, which is almost unchanged shown in Fig 5(a). At the same time, no apparent changes are observed in the periodic I - T photoresponse [Fig. 5(b)], which imply a high stability and robustness of the encapsulated device. The solid-state semiconductor detectors, such as Si, Se, Cd(Zn)Te, and perovskites, which are widely studied in X-ray detection, are also materials sensitive to visible light due to their small bandgaps. Therefore, these materials are more susceptible to the external electromagnetic radiation. However, the X-ray transmissive encapsulation filled with nitrogen is capable of blocking the ambient light and providing an inert atmosphere for the detector. The detection sensitivities of the encapsulated device as a function of radiation dose rates and bias voltages are shown in Fig. 5(c) and (d), respectively. The encapsulated device still maintains excellent detection sensitivity after two months of storage, which indicates the favorable operability of our packaging module.

IV. CONCLUSION

In summary, we proposed a new strategy to fabricate a high-performance environmental-friendly X-ray detector by using all-inorganic lead-free double perovskite film in radiation detection. Here, for the first time, the highly sensitive $\text{Cs}_2\text{AgBiBr}_6$ film X-ray detector with a photoconductive planar architecture is successfully demonstrated and encapsulated using a metal casing with a $100\text{-}\mu\text{m}$ -thick Be window. The high average atomic number, long carrier diffusion length and lifetime, as well as the high intrinsic resistance make the $\text{Cs}_2\text{AgBiBr}_6$ film well suitable for direct X-ray detection. In this article, high-quality $\text{Cs}_2\text{AgBiBr}_6$ films are obtained through the systematical study of the best moment of dripping the antisolvent IPA during the spin coating process. It has been demonstrated that with the delay of the antisolvent IPA dripping time, the films are likely to exhibit larger grain size and higher coverage, which is conducive to the improvement of device performance. The photophysical investigations reveal that the $\text{Cs}_2\text{AgBiBr}_6$ film has a long carrier diffusion length of approximately 700 nm and a long carrier lifetime of nearly 750 ns at room temperature. In terms of encapsulation, the X-ray transmissive packaging module filled with nitrogen is capable of blocking the external ambient and providing an inert atmosphere for the detector. Benefiting from the excellent properties of the $\text{Cs}_2\text{AgBiBr}_6$ film and the stable ambient provided by the packaging module, the resulting device exhibits attractive X-ray detection capabilities with a detection sensitivity up to $1 \times 10^4 \mu\text{CGy}_{\text{air}}^{-1}\text{cm}^{-2}$, which is about a thousand times higher than the sensitivity achieved with commercial a-Se X-ray detectors. Besides, a minimum detectable dose rate of $145.2 \text{ nGy}_{\text{air}}\text{s}^{-1}$ is also achieved, showing the potential to significantly reduce the radiation dose of X-ray. Besides, the encapsulated device maintains superior detection performance after 2 months of storage, indicating the favorable reliability of the encapsulated device. The superior detection performance of the $\text{Cs}_2\text{AgBiBr}_6$ film will motivate new strategies to achieve high-performance X-ray detectors by

utilizing all-inorganic lead-free perovskite film, promoting its application in radiation electronics.

REFERENCES

- [1] P. S. Yoon, "Customisable X-ray fluorescence photodetector with sub-micron sensitivity using a ring array of silicon p-i-n diodes," *Sci. Rep.*, vol. 8, no. 1, p. 15926, Oct. 2018, doi: [10.1038/s41598-018-33966-y](https://doi.org/10.1038/s41598-018-33966-y).
- [2] S. O. Kasap, "X-ray sensitivity of photoconductors: Application to stabilized a-Se," *J. Phys. D, Appl. Phys.*, vol. 33, no. 21, p. 2853, 2000, doi: [10.1088/0022-3727/33/21/21326](https://doi.org/10.1088/0022-3727/33/21/21326).
- [3] V. Dvoryankin, G. Dvoryankina, A. Kudryashov, A. Petrov, V. Golyshev, and S. Bykova, "X-ray sensitivity of Cd_{0.9}Zn_{0.1}Te detectors," *Tech. Phys.*, vol. 55, no. 2, pp. 306–308, 2010, doi: [10.1016/s1003-6326\(16\)64330-3](https://doi.org/10.1016/s1003-6326(16)64330-3).
- [4] J. H. Won *et al.*, "The X-ray sensitivity of semi-insulating polycrystalline CdZnTe thick films," *Nucl. Instrum. Methods Phys. Res. A, Accel. Spectrom. Detect. Assoc. Equip.*, vol. 591, no. 1, pp. 206–208, Jun. 2008, doi: [10.1016/j.nima.2008.03.057](https://doi.org/10.1016/j.nima.2008.03.057).
- [5] D. M. Trucchi, P. Allegrini, A. Bellucci, P. Calvani, A. Galbiati, and M. Girolami, "Resistant and sensitive single-crystal diamond dosimeters for ionizing radiation," *Nucl. Instrum. Methods Phys. Res. A, Accel. Spectrom. Detect. Assoc. Equip.*, vol. 718, pp. 373–375, Aug. 2013, doi: [10.1016/j.nima.2012.10.095](https://doi.org/10.1016/j.nima.2012.10.095).
- [6] A. Owens, "Semiconductor materials and radiation detection," *J. Synchrotron Radiat.*, vol. 13, no. 2, pp. 143–150, Mar. 2006, doi: [10.1107/s0909049505033339](https://doi.org/10.1107/s0909049505033339).
- [7] Z. He, W. Li, G. Knoll, D. Wehe, and C. Stahle, "Measurement of material uniformity using 3-D position sensitive CdZnTe gamma-ray spectrometers," *Nucl. Instrum. Methods Phys. Res. A, Accel. Spectrom. Detect. Assoc. Equip.*, vol. 441, no. 3, pp. 459–467, 2000, doi: [10.1016/s0168-9002\(99\)00860-8](https://doi.org/10.1016/s0168-9002(99)00860-8).
- [8] R. D. Evans and A. Noyau, *The Atomic Nucleus*, vol. 582. New York, NY, USA: McGraw-Hill, 1955.
- [9] S. Yakunin *et al.*, "Detection of X-ray photons by solution-processed lead halide perovskites," *Nature Photon.*, vol. 9, p. 444, May 2015, doi: [10.1038/nphoton.2015.82](https://doi.org/10.1038/nphoton.2015.82).
- [10] Y. C. Kim *et al.*, "Printable organometallic perovskite enables large-area, low-dose X-ray imaging," *Nature*, vol. 550, no. 7674, pp. 87–91, 2017, doi: [10.1038/nature24032](https://doi.org/10.1038/nature24032).
- [11] S. Shrestha *et al.*, "High-performance direct conversion X-ray detectors based on sintered hybrid lead triiodide perovskite wafers," *Nature Photon.*, vol. 11, no. 7, pp. 436–440, 2017, doi: [10.1038/nphoton.2017.94](https://doi.org/10.1038/nphoton.2017.94).
- [12] H. Wei *et al.*, "Sensitive X-ray detectors made of methylammonium lead tribromide perovskite single crystals," *Nature Photon.*, vol. 10, p. 333, Mar. 2016, doi: [10.1038/nphoton.2016.41](https://doi.org/10.1038/nphoton.2016.41).
- [13] W. Wei *et al.*, "Monolithic integration of hybrid perovskite single crystals with heterogenous substrate for highly sensitive X-ray imaging," *Nature Photon.*, vol. 11, p. 315, Apr. 2017, doi: [10.1038/nphoton.2017.43](https://doi.org/10.1038/nphoton.2017.43).
- [14] H. Wei *et al.*, "Dopant compensation in alloyed CH₃NH₃PbBr_{3-x}Cl_x perovskite single crystals for gamma-ray spectroscopy," *Nat. mater.*, vol. 16, no. 8, pp. 826–833, 2017, doi: [10.1038/nmat4927](https://doi.org/10.1038/nmat4927).
- [15] M. D. Birowosuto *et al.*, "X-ray scintillation in lead halide perovskite crystals," *Sci. Rep.*, vol. 6, no. 1, p. 37254, Dec. 2016, doi: [10.1038/srep37254](https://doi.org/10.1038/srep37254).
- [16] S. Yakunin *et al.*, "Detection of gamma photons using solution-grown single crystals of hybrid lead halide perovskites," *Nature Photon.*, vol. 10, no. 9, pp. 585–589, 2016, doi: [10.1038/nphoton.2016.139](https://doi.org/10.1038/nphoton.2016.139).
- [17] C. C. Stoumpos *et al.*, "Crystal growth of the perovskite semiconductor CsPbBr₃: A new material for high-energy radiation detection," *Crystal Growth Des.*, vol. 13, no. 7, pp. 2722–2727, Jul. 2013, doi: [10.1021/cg400645t](https://doi.org/10.1021/cg400645t).
- [18] M. Chen *et al.*, "Highly stable and efficient all-inorganic lead-free perovskite solar cells with native-oxide passivation," *Nature Commun.*, vol. 10, no. 1, p. 16, Jan. 2019, doi: [10.1038/s41467-018-07951-y](https://doi.org/10.1038/s41467-018-07951-y).
- [19] F. Wang *et al.*, "Organic cation-dependent degradation mechanism of organotin halide perovskites," *Adv. Funct. Mater.*, vol. 26, no. 20, pp. 3417–3423, May 2016, doi: [10.1002/adfm.201505127](https://doi.org/10.1002/adfm.201505127).
- [20] G. Volonakis *et al.*, "Cs₂InAgCl₆: A new lead-free halide double perovskite with direct band gap," *J. Phys. Chem. Lett.*, vol. 8, no. 4, pp. 772–778, Feb. 2017, doi: [10.1021/acs.jpclett.6b02682](https://doi.org/10.1021/acs.jpclett.6b02682).
- [21] E. T. McClure, M. R. Ball, W. Windl, and P. M. Woodward, "Cs₂AgBiX₆ (X = Br, Cl): New visible light absorbing, lead-free halide perovskite semiconductors," *Chem. Mater.*, vol. 28, no. 5, pp. 1348–1354, Mar. 2016, doi: [10.1021/acs.chemmater.5b04231](https://doi.org/10.1021/acs.chemmater.5b04231).
- [22] W. Pan *et al.*, "Cs₂AgBiBr₆ single-crystal X-ray detectors with a low detection limit," *Nature Photon.*, vol. 11, no. 11, pp. 726–732, 2017, doi: [10.1038/s41566-017-0012-4](https://doi.org/10.1038/s41566-017-0012-4).
- [23] W. Yuan *et al.*, "In situ regulating the order-disorder phase transition in Cs₂AgBiBr₆ single crystal toward the application in an X-ray detector," *Adv. Funct. Mater.*, vol. 29, no. 20, May 2019, Art. no. 1900234, doi: [10.1002/adfm.201900234](https://doi.org/10.1002/adfm.201900234).
- [24] J. A. Steele *et al.*, "Photophysical pathways in highly sensitive Cs₂AgBiBr₆ double-perovskite single-crystal X-ray detectors," *Adv. Mater.*, vol. 30, no. 46, Nov. 2018, Art. no. 1804450, doi: [10.1002/adma.201804450](https://doi.org/10.1002/adma.201804450).
- [25] I. Clairand *et al.*, "Use of active personal dosimeters in interventional radiology and cardiology: Tests in laboratory conditions and recommendations—ORAMED project," *Radiat. Meas.*, vol. 46, no. 11, pp. 1252–1257, Nov. 2011, doi: [10.1016/j.radmeas.2011.07.008](https://doi.org/10.1016/j.radmeas.2011.07.008).
- [26] M. J. Berger *et al.* (2013). *XCOM: Photon Cross Sections Database: NIST Standard Reference Database 8*. [Online]. Available: <https://www.nist.gov/pml/xcom-photon-cross-sections-database>
- [27] J. Yang *et al.*, "Stable, high-sensitivity and fast-response photodetectors based on lead-free Cs₂AgBiBr₆ double perovskite films," *Adv. Opt. Mater.*, vol. 7, May 2019, Art. no. 1801732, doi: [10.1002/adom.201801732](https://doi.org/10.1002/adom.201801732).
- [28] W. Ning *et al.*, "Long electron-hole diffusion length in high-quality lead-free double perovskite films," *Adv. Mater.*, vol. 30, no. 20, May 2018, Art. no. 1706246, doi: [10.1002/adma.201706246](https://doi.org/10.1002/adma.201706246).
- [29] M. Chen *et al.*, "Cesium titanium (IV) bromide thin films based stable lead-free perovskite solar cells," *Joule*, vol. 2, no. 3, pp. 558–570, Mar. 2018, doi: [10.1016/j.joule.2018.01.009](https://doi.org/10.1016/j.joule.2018.01.009).
- [30] H. Zhang *et al.*, "X-ray detector based on all-inorganic lead-free Cs₂AgBiBr₆ perovskite single crystal," *IEEE Trans. Electron Devices*, vol. 66, no. 5, pp. 2224–2229, May 2019, doi: [10.1109/TED.2019.2903537](https://doi.org/10.1109/TED.2019.2903537).
- [31] B. L. Henke, E. M. Gullikson, and J. C. Davis, "X-ray interactions: Photoabsorption, scattering, transmission, and reflection at E = 50–30,000 eV, Z = 1–92," *At. Data Nucl. Data Tables*, vol. 54, no. 2, pp. 181–342, Jul. 1993, [Online]. Available: http://henke.lbl.gov/optical_constants/ and doi: [10.1006/adnd.1993.1013](https://doi.org/10.1006/adnd.1993.1013).
- [32] J. He *et al.*, "Synergetic effect of silver nanocrystals applied in PbS colloidal quantum dots for high-performance infrared photodetectors," *ACS Photon.*, vol. 1, no. 10, pp. 936–943, Oct. 2014, doi: [10.1021/ph500227u](https://doi.org/10.1021/ph500227u).
- [33] J. H. Hubbel and S. M. Seltzer, "Tables of X-ray mass attenuation coefficients and mass energy-absorption coefficients 1 keV to 20 meV for elements Z = 1 to 92 and 48 additional substances of dosimetric interest," *Radiat. Phys. Division, PML, NIST, Gaithersburg, MD, USA, Tech. Rep. NISTIR 5632*, 2004. [Online]. Available: <https://www.nist.gov/pml/x-ray-mass-attenuation-coefficients>
- [34] *Radiation Safety For Personnel Security Screening Systems Using X-ray or Gamma Radiations*, document A. H. N43.17, 2009. [Online]. Available: <http://hps.org/hpsc/>
- [35] J. M. Boone and J. A. Seibert, "An accurate method for computer-generating tungsten anode X-ray spectra from 30 to 140 kV," *Med. Phys.*, vol. 24, no. 11, pp. 1661–1670, Nov. 1997, doi: [10.1118/1.597953](https://doi.org/10.1118/1.597953).
- [36] M. Thompson, S. L. R. Ellison, and R. Wood, "Harmonized guidelines for single-laboratory validation of methods of analysis (IUPAC technical report)," *Pure Appl. Chem.*, vol. 74, no. 5, pp. 835–855, Jan. 2002, doi: [10.1351/pac200274050835](https://doi.org/10.1351/pac200274050835).
- [37] R. Zhuang *et al.*, "Highly sensitive X-ray detector made of layered perovskite-like (NH₄)₃Bi₂I₉ single crystal with anisotropic response," *Nature Photon.*, vol. 13, no. 9, pp. 602–608, Sep. 2019, doi: [10.1038/s41566-019-0466-7](https://doi.org/10.1038/s41566-019-0466-7).